



# A heterogeneous multiscale MPFA method for single-phase flows in porous media with inertial effects

Sergey Alyaev<sup>1</sup> · Eirik Keilegavlen<sup>2</sup> · Jan M. Nordbotten<sup>2,3</sup>

Received: 20 October 2017 / Accepted: 10 October 2018 / Published online: 26 November 2018  
© The Author(s) 2018

## Abstract

Upscaling of flow from pore to Darcy scale is a long-standing research field within flow in porous media. It is well known that non-linearities can occur in near-well regions and high-porosity or fractured media. At the same time, the upscaled non-linear effects associated with high flow rates are hard to quantify a priori with single-scale models. Advances in pore-scale imaging combined with increased computational have made flow simulations in small pore-scale domain feasible, but computations on domains larger than at most a few centimeters are still elusive. In this work, we present a multiscale simulation framework that automatically adapts to non-linear effects as they arise. We formulate a control volume heterogeneous multiscale method (CVHMM) by coupling of a Darcy-scale control volume method with a constitutive relation that is captured based on the fine-scale physics. While the CVHMM formulation works with arbitrary upscaled laws, we emphasize its ability to be applied in fully discrete multiscale context, in particular when a finite element solver is used for solving Navier-Stokes equations on the fine-scale pore geometry. Previous versions of CVHMM are consistent only when the coarse grid is aligned with the upscaled permeability. Herein, we generalize CVHMM by introducing a new coarse solver, thus significantly improving the applicability of the method. The presented method is applied to study flow in near-well regions, as well as media with fractures and irregular grain shapes. The examples show that the method successfully copes with general grids and pore geometries and handles flows with varying degree of non-linearities even outside the domain of applicability of classical upscaled models. In terms of computational efficiency, the method seamlessly localizes computations to regions where non-linear effects are important.

**Keywords** Pore scale · Numerical upscaling · Hybrid multiscale method · Near-well flow

## 1 Introduction

Flow in porous media is commonly modeled by Darcy's law, which postulates a linear relationship between the fluid flux and pressure gradient. The linear proportionality constant is approximated as the ratio of a medium property (permeability) and a fluid property (viscosity). In effect, Darcy's law replaces flow in the geometry

defined by the pore channels by an upscaled constitutive law. Historically, the permeability has been estimated by laboratory experiments. Today, progress in pore-scale imaging, e.g., [10, 11, 18, 53], provides highly resolved information on both pore-scale geometry and dynamic processes, while advancement in numerical simulation allows mimicking this dynamics to an increased degree [31, 36, 42, 54]. This allows for novel insight into pore-scale processes and also serves as a starting point for numerical upscaling to Darcy-scale properties [14, 28, 35, 38, 40].

A common assumption in numerical upscaling is that the pore-scale flow is linear, and thus can be modeled by Stokes equation. In this case, the linear relation in Darcy's law can be theoretically justified [26, 51]. The accuracy of this assumption depends on the imposed pressure gradients, but also on the configuration of the porous structure, which determines the resistance to flow. In practice, while the assumption of linear flow is suitable in a wide range of applications [55], it is insufficient for high flow rates, as

---

✉ Sergey Alyaev  
Sergey.Alyaev@norceresearch.no

<sup>1</sup> NORCE Norwegian Research Centre, Nygårdsgaten 112, 5008 Bergen, Norway

<sup>2</sup> Department of Mathematics, University of Bergen, Bergen, Norway

<sup>3</sup> Department of Civil and Environmental Engineering, Princeton University, Princeton, NJ, USA

can occur in near-well regions [47], fractures [45], soil-rock mixtures [50], and industrial filters [27].

At higher flow rates, the non-linear inertia term in the Navier-Stokes equations are not negligible at the fine scale. On the coarse scale, the inertia term manifests itself as an increased resistance to flow. The reduction in flow is commonly modeled heuristically by Forchheimer's law, which amends Darcy's equation with a term representing the square of the velocity, multiplied by a tuning parameter. The non-linear term is dependent on the flow rate, which in itself is influenced by non-local effects. Hence, special numerical methods should be used for the coarse scale problem [24]. Although Forchheimer's law can be theoretically justified in some cases [20, 52], like the Darcy's law, it has a limited range of validity [13, 16, 38, 44], and generalized extensions were proposed in recent years [38].

The process of selecting the best upscaling, pre-computation of necessary tuning parameters, and adjusting the coarse-scale methods to cope with it is an ongoing research.

The challenges related to the unknown flow regimes can be circumvented by applying multiscale simulation techniques which combine fine- and coarse-scale simulations. In [42], trinary image segmentation of the pore scale was used to divide the void into porous and free-flow regions, where Darcy and Stokes equation were solved, respectively. In [46], a similar hybrid method, which uses fine-scale pore-network simulation in the near-well region, is presented. The method allows to capture the non-Darcy behavior where it is most pronounced. Another multi-physics approach is to decompose the pore-scale domain into subdomains and model long-range communication by a coarse-scale Darcy solver [48, 49].

Our main interest herein is in obtaining an effective discrete representation of non-linear upscaled Darcy-scale models, that is is flexible with respect to constitutive relationships and allows for either a priori derived non-linear upscaled laws such as Forchheimer, or on-demand upscaling of pore-scale computations. This is possible through several computational approaches. A finite-element approach of mortar coupling was investigated in [15] and further applied to solve a challenges of upscaling dynamics of non-Newtonian fluids in [34]. In [43], the authors developed a multiscale method that uses local pore-network simulations to dynamically estimate relative permeability. In this paper, we focus on the framework of the heterogeneous multiscale method (HMM) [23].

For instance, it can be applied to get the relation between pressure drops and fluxes, by solving the flow equations locally in certain quadrature points. The framework allows for flexibility of a fine-scale solver that can be an analytical model (resulting in traditional upscaling, see, e.g., [26]), or a numerical model such as a pore-network model [21, 22],

or a Navier-Stokes solver [8, 9], resulting in a fully discrete multiscale method.

The latter approach, termed the control volume heterogeneous multiscale method (CVHMM), is the subject of this paper. The method retains the advantages of control volume methods (CVM) in terms of being both locally mass conservative, as well as having only pressure as discrete variables on the coarse scale<sup>1</sup>.

Simultaneously, it allows for the flexibility of HMM when it comes to the fine-scale-based flux approximation such that the constitutive laws can be specified either a priori or through local calculations on the fine scale. In the latter case, the fine-scale equations are only solved on small patches around the quadrature points ensuring relatively low computational cost, while maintaining reasonable accuracy due to the structure of the coarse-scale problem (see [4, 5, 9] for error estimates).

Previous CVHMM have been deficient in that only simple two-point relationships have been used to approximate the pressure gradient in the constitutive laws [9]. This approximation is only accurate if the upscaled flow aligns with the gradient, which depends on the precise micro-scale geometry. As such, previous CVHMM are not two-scale convergent for general micro-scale configurations. To remedy this situation, we herein consider a coarse-scale control-volume method based on the multi-point flux approximation (MPFA) [1, 3, 25] methods. In addition to providing a consistent macro-scale representation of anisotropic constitutive laws, these methods have the additional advantage of allowing for flexible grid configurations, including adaptive grids with hanging nodes.

The novel contribution of this paper can thus be summarized as follows: We present a heterogeneous multiscale MPFA method for steady-state single-phase flows in porous media, which relaxes all a priori assumptions about the anisotropy of the upscaled constitutive laws. Moreover, as we demonstrate in our numerical examples, our approach naturally allows for complex grids and non-linear laws with pronounced inertial forces including directionally dependent upscaled flow resistance.

The paper is organized as follows. We start by summarizing the models on both Darcy scale and pore scale in Section 2. Further, Section 3 is dedicated to presentation of the CVHMM framework. The convergence properties of the fully discrete method based on MPFA are verified against error estimates from [3, 9] in the [Appendix](#).

The numerical simulations of applications with non-linear flows are provided in Section 4. The paper is summarized in Section 5.

<sup>1</sup> The method is also referred to as the finite volume method (FVM), see, e.g., [48]. We note that CVM and FVM are complete synonyms.

## 2 Model problem

Our goal is to solve single-phase flow problems on the Darcy scale without making a priori assumptions on the flow model, specifically on constitutive equations for the flux. To that end, we follow the HMM framework, and define a coarse-scale model, which only assumes conservation of mass on the Darcy scale [23]. To close the coarse model, we couple it to a pore-scale model governed by the Navier-Stokes equations. In this section, the model equations on the two scales are presented without introducing any discretization. We also prepare the ground for communication between the scales that is needed for the multiscale method described in the next section.

We remark that even though the presentation emphasizes the most general case of a pore-scale model with Navier-Stokes equations, the general approach allows for any fine-scale model which can provide an upscaled flux based on a prescribed pressure gradient. In particular, any a priori derived (or experimentally measured) constitutive law can be used, in which case the method reduces to a single (coarse)-scale model for non-linear single-phase flow.

### 2.1 Darcy-scale model

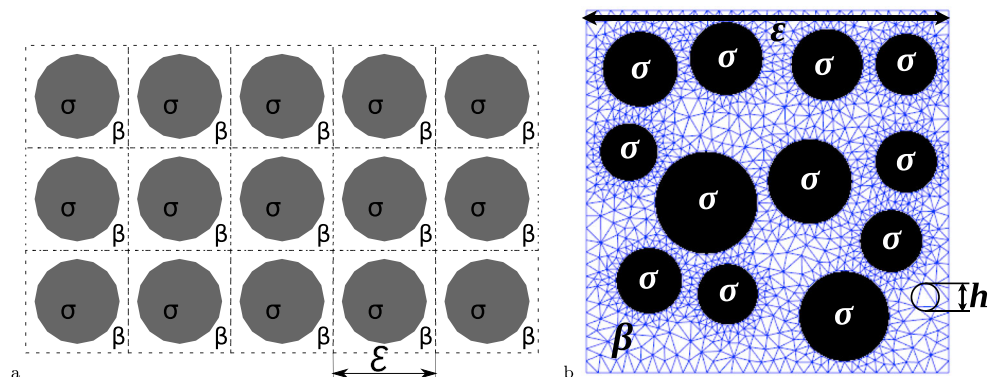
Our coarse-scale model is based on conservation of mass of the fluid, which under the assumption of incompressibility reads

$$\int_{\partial\tau} \mathbf{u} \cdot \mathbf{n} dS = \int_{\tau} f dV. \tag{1}$$

Here,  $\tau$  is an arbitrary volume with boundary  $\partial\tau$ ,  $\mathbf{u}$  is the flux density, and  $f$  is the volumetric source per unit volume.

The equation for Darcy-scale conservation of mass (1) should be accompanied with a relation between the flow velocity  $\mathbf{u}$  and state variables, in practice the coarse-scale pressure  $P$ . Traditionally, this is modeled by Darcy’s law as a linear relation between pressure drop and flux. Herein, we replace this assumption with an appropriate constitutive relation upscaled from a fine-scale model as discussed below.

**Fig. 1** A simple periodic structure forming coarse scale domain (a) and an example of a more complex fine scale cell problem with triangulation (b)



### 2.2 Pore-scale model

The traditional approach to pore-scale modeling assumes slow flow governed by Stokes equation, which, when upscaled results in Darcy’s law [26]. Herein, we instead model pore-scale flow of the fluid by the Navier-Stokes equations, which capture a wider range of flow regimes.

Compared to Stokes flow, which is fully dominated by viscous forces, Navier-Stokes equations correctly reproduce inertia effects observed in faster flows.

Motivated by results from homogenization, e.g., [26], we solve the pore-scale problem on local patches of size  $\varepsilon$ , which corresponds to the period of the structure of the porous medium (see Fig. 1), or equivalently of the size of the natural representative elementary volume. We assume that  $\varepsilon$  is much smaller than the size of the coarse-scale domain.

The local problem is stated on the unit cell  $\omega$ , composed of the pore space  $\beta$  and solid inclusions  $\sigma$ ,

$$\omega = \beta \cup \sigma, \tag{2}$$

(see Fig. 1). The Navier-Stokes flow equations for the pore scale can be formulated as follows. Conservation of mass for an incompressible fluid is expressed as divergence free flow for the fine-scale velocity  $\mathbf{v}$ :

$$\nabla \cdot \mathbf{v} = 0, \text{ in } \beta. \tag{3}$$

It is coupled with the non-linear equation for momentum conservation which due to separation of scales can be solved in the steady state form:

$$\rho (\mathbf{v} \cdot \nabla \mathbf{v}) = -\nabla p + \mu \Delta \mathbf{v} + \tilde{\mathbf{f}}, \text{ in } \beta, \tag{4}$$

where  $p$  is pressure,  $\mu$  is viscosity, and  $\tilde{\mathbf{f}}$  represents density of body forces. On the boundaries  $\partial\omega$ , periodic conditions are assigned, while the boundary of the solid inclusions  $\partial\sigma$  are assigned no-flow conditions. The volumetric force  $\tilde{\mathbf{f}}$  acting on the fluid is composed of the coarse-scale forces (in our case pressure gradients), re-scaled to the local domain. Thus the fine-scale velocity field can be thought of as a result of the fine-scale response given a coarse-scale pressure gradient for a certain pore geometry. The absence

of explicit time dependency in (4) means that the fine-scale flow responds instantaneously to changes in the coarse scale conditions. While  $\tilde{f}$  is constant in the pore-scale problem on a unit cell  $\beta$ , coarse-scale dynamics make it vary between unit cells. The result is a set of fine-scale problems to be solved for different flow regimes.

The Darcy-scale velocity  $\mathbf{u}$  at any point  $x$ , required for closing the coarse system, is the spatial average of the fine-scale velocity field over the periodic unit cell

$$\mathbf{u}(\nabla P; x) = \frac{\int_{\beta(x)} \mathbf{v}(\nabla P; y) dy}{\int_{\omega(x)} dy}, \quad (5)$$

where  $\beta(x)$  is the fluid part of the periodic cell located around a coarse point  $x$ . If the Darcy velocity is linear with respect to  $\nabla P$ , the proportionality constant is the permeability [26].

The theoretical homogenization results presented in [26] show that for periodic porous media the requirement of periodicity of velocity and pressure on the boundaries of periodic domain results in two-scale convergence. As was shown in [4, 6, 7, 9, 21], this formulation is suitable for the construction of heterogeneous multiscale methods. As in these previous works, we assume that the pore geometry (grain structure) is known and that it is periodic with period  $\varepsilon$  on the coarse grid blocks. At the same time, we note that the methodology is applicable to non-periodic media (see, e.g., [6]).

### 3 Two-scale numerical discretization

The model outlined in the previous section, with coarse-scale conservation coupled with fluxes from fine-scale computations, provides an attractive formulation of non-standard Darcy-scale models from the perspective of multi-scale discretization.

In this section, we discuss the control volume discretization of the coarse scale and the coupling between the scales. The general coarse-scale discretization based on cell centered control volumes is introduced in Section 3.1. The coupling between coarse and fine-scale computations requires interpolation of the cell center pressures, and the localization of quadrature points wherein the fine-scale solver is invoked. Our method, presented in Section 3.2, is an extension of the MPFA L-method [3]. This gives our method superior ability to handle rough grids, including hanging nodes, and be consistent with linear and non-linear anisotropies as shown in Section 4. The final ingredient of the method, the estimation of a Darcy-scale discrete velocity is introduced in Section 3.3 and is flexible with respect to the estimation operator.

In the subsection, we define the estimation operator and consider two natural options: an upscaled constitutive relationship such as Forchheimer's law, and a discrete fine-scale solver (based on finite-element solver of Navier-Stokes' equations).

Section 3.4 summarizes the implementation CVHMM algorithm.

#### 3.1 Coarse-scale discretization

In applications, the flow equation is commonly coupled to a non-linear transport equation. To avoid instabilities in the transport solver, it is common practice to enforce the conservation property on the flow field by employing a conservative discretization. To that end, our coarse solver is designed based on control volume principles and enforces (1) on a discrete cell level as

$$\int_{\partial\tau_i} \mathbf{u}_{h,i} \cdot \mathbf{n} ds = \sum_k \int_{\partial\tau_{i,k}} \mathbf{u}_{h,i} \cdot \mathbf{n}_{i,k} ds = \int_{\tau_i} f dx, \quad \forall \tau_i. \quad (6)$$

Here,  $\mathbf{u}_h$  is the discretized velocity,  $\tau_i$  is a control volume with normal vector  $\mathbf{n}$ ;  $\partial\tau_i$  is its boundary split into its edges with neighboring cells,  $k$ ; and  $\mathbf{n}_{i,k}$  is a unit normal pointing from cell  $i$  to  $k$ . Furthermore, the control volume method ensures that for any pair of control volumes  $\tau_i$  and  $\tau_k$  which share a common edge  $\partial\tau_{i,k}$ , flow is conserved across that edge, by requiring that

$$u_j \equiv \int_{\partial\tau_{i,k}} \mathbf{u}_{h,i} \cdot \mathbf{n}_{i,k} ds = - \int_{\partial\tau_{k,i}} \mathbf{u}_{h,k} \cdot \mathbf{n}_{k,i} ds, \quad (7)$$

where  $u_j$  is the control volume flux between volumes  $i$  and  $k$ . As primary variables in our formulation, we choose the cell center pressures, and let  $P_i$  denote the pressure in control volume  $\tau_i$ . To progress, we need to specify how the fluxes  $u_j$  are related to the primary variables.

#### 3.2 Coarse flux approximation and quadrature rule

We design our pressure interpolation and flux approximation based on two principles. First, our method should capture discontinuities in pressure associated with discontinuities in the grain structure (permeability on the Darcy scale). We assume that the grain structure is constant within each coarse cell, and that discontinuities are resolved by the cell boundaries. Flux continuity over the boundary then implies that the pressure gradient can be discontinuous, and must be treated accordingly in the numerical approximation. Second, the method should be consistent for general grain configurations relative to the coarse-scale grid; that is, we put no restrictions that the upscaled permeability is aligned with the coarse grid. This implies that the discretization should represent any linear pressure variation.

Motivated by the above points, we design our method on the class of multi-point flux approximation (MPFA) methods; specifically, we have implemented a variant related to the so-called MPFA L-method [3]. MPFA methods represent the pressure as general linear functions on sub-cells (defined below), with possible jumps in the gradient over cell boundaries. Together, this allows for a consistent approximation; notably, it generalizes the previous formulation of CVHMM [8, 9], which used two-point flux approximation (TPFA) for the flux estimation. Unlike TPFA, MPFA-type schemes do not require the coarse-scale grid to be aligned with orientation of permeability tensor, thus removing a crucial restriction of the simpler method [1]. The HMM formulation of the MPFA method generalizes the well established single-scale version, by allowing the velocity to be computed dynamically using a data estimation operator, rather than via Darcy’s law with a known permeability.

In this section, we briefly review HMM formulation of TPFA and describe HMM MPFA as its generalization. Both methods approximate a flux across a coarse edge by introducing auxiliary variables and eliminating them locally constrained by the continuity of the basis functions. However, unlike the single-scale versions of the method, this elimination requires solving a non-linear equations and cannot be written in a closed form. The local regions that are considered during such local computation of the fluxes are termed interaction regions (see illustration in Fig. 2). Each of the methods is defined by the shape of interaction regions, positions of auxiliary points and constraints required for their elimination.

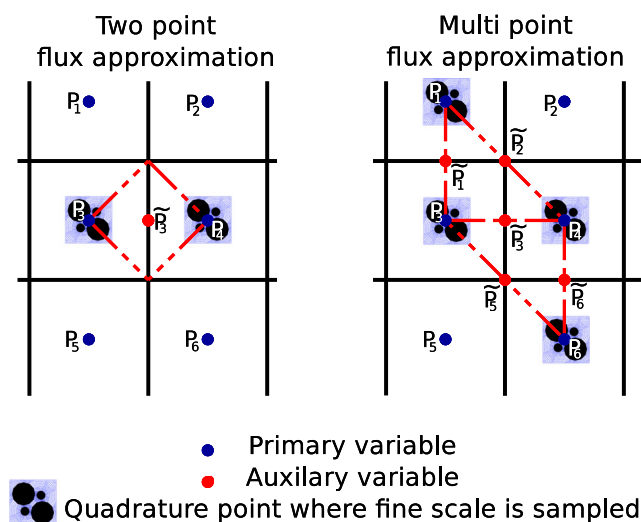


**Fig. 2** Quadrature rules and coarse-scale discretizations that can be applied with CVHMM. Black lines indicate coarse grid; red lines show local interaction region where interpolation is performed. Fine-scale domains with blue fine-scale grid are shown where the quadrature points would be sampled for each method. For convenience of explanation, the primary and auxiliary variables are locally numbered

### 3.2.1 Two-point flux approximation

The TPFA (see stencil on the left in Fig. 2) computes the flux across the middle edge ( $u_{3,4}$ ) from the pressures (primary variables) in the two adjacent cell centers ( $P_3$  and  $P_4$ ).

The method is defined as follows. We introduce an auxiliary pressure in the middle of the edge and denote it as  $\tilde{P}_3$ .

As in single-scale TPFA, we assume that for each sub-cell of interaction region pressure is defined as linear function connecting the primary variables with the edge center ( $P_3$  and  $\tilde{P}_3$  and  $P_4$ , respectively).

This gives two constant pressure gradients using which the Darcy-scale velocities in each sub-cell can be estimated from fine scale model (5). The multiscale flow velocity estimation process is detailed in Section 3.3. We denote the local velocities by  $\mathbf{u}_{h,3}(P_3, \tilde{P}_3)$  and  $\mathbf{u}_{h,4}(\tilde{P}_3, P_4)$ . Constant pressure gradients imply constant that  $\mathbf{u}_{h,3}$  and  $\mathbf{u}_{h,4}$  are also constant.

The flux across the edge  $u_{3,4}$  can be computed by imposing mass conservation across the interface (7) and thus eliminating the auxiliary pressure  $\tilde{P}_3$ :

$$u_{3,4} \equiv |\partial \tau_{3,4}| \mathbf{u}_{h,3}(P_3, \tilde{P}_3) \cdot \mathbf{n}_{3,4} = -|\partial \tau_{3,4}| \mathbf{u}_{h,4}(\tilde{P}_3, P_4) \cdot \mathbf{n}_{4,3}. \tag{8}$$

Note that in CVHMM, the non-linear (8) is solved locally by a Newton-type method.

By construction, the TPFA cannot represent the effect of the full pressure gradient; for instance for the Cartesian grid depicted in Fig. 2, the component of the gradient that is parallel to the edge will not be represented in the interpolation. As a result, two-point schemes are prone to grid-orientation effects and can converge to a wrong solution.

### 3.2.2 Multi-point flux approximation L-method

We amend this shortcoming by using MPFA L-method [3] (see Fig. 2 (right)). Compared to the two-point flux, the stencil used in the multi-point approximations can represent components of the pressure gradient that are not aligned with the grid, and is thus a consistent approximation. The particular choice of an L-method allows for treatment of grid adaptivity, hanging nodes and more general polygonal cells (see, e.g., [3, 25]). The importance of these features is demonstrated in our numerical examples. We emphasize that our method is also applicable to other multi-point stencils [2], although we do not pursue that option here.

The L-method on a quadrilateral grid can be defined as follows. First, we divide each cell into four sub-cells (one

for each vertex). The computation is then carried out on L-shaped interaction regions, made up of three neighboring sub-cells, centered around a vertex. Figure 2 on the right shows two interaction regions needed for computation of  $u_{3,4}$ : enclosed in points  $P_1, \tilde{P}_1, P_3, \tilde{P}_3, P_4, \tilde{P}_2$  and  $P_5, \tilde{P}_5, P_4, \tilde{P}_3, P_3, \tilde{P}_3$ .<sup>2</sup>

We demonstrate the MPFA L-method on the example of the first region.

As in TPFa, the pressure is assumed to be linear in every sub-cell corresponding to coarse discretization. Thus, the pressure gradient is constant on each of the three sub-cells  $((P_1, \tilde{P}_1, \tilde{P}_2); (\tilde{P}_1, P_3, \tilde{P}_3, \tilde{P}_2); (\tilde{P}_3, P_4, \tilde{P}_2))$ . As before, the pressure gradients are used to compute the constant local flow velocities  $\mathbf{u}_1, \mathbf{u}_3$ , and  $\mathbf{u}_4$  by applying (5) at the quadrature points corresponding to primary variables  $P_1, P_3$  and  $P_4$  (see Fig. 2). The discrete local velocities are the functions of discrete pressures:

$$\begin{aligned} \mathbf{u}_1 &= \mathbf{u}(P_1, \tilde{P}_1, \tilde{P}_2), \\ \mathbf{u}_3 &= \mathbf{u}(P_3, \tilde{P}_1, \tilde{P}_3), \\ \mathbf{u}_4 &= \mathbf{u}(P_4, \tilde{P}_2, \tilde{P}_3), \end{aligned}$$

where each velocity depends on two auxiliary variables and one primary variable defining a unique gradient in 2D. Analogously to Eq. 8, we want to eliminate auxiliary variables  $\tilde{P}_i$  locally to find the fluxes across edges. In this case, however, the conservation principles would be enforced on each half edge that enters the interaction region. We denote the fluxes across the half-edges in the region of interest as  $u_{1,3}^{1/2}$  and  $u_{3,4}^{1/2}$  and they satisfy the equations:

$$\begin{aligned} u_{1,3}^{1/2} &\equiv \frac{1}{2} |\partial\tau^{1,3}| \mathbf{u}_1(P_1, \tilde{P}_1, \tilde{P}_2) \cdot \mathbf{n}_{1,3} \\ &= -\frac{1}{2} |\partial\tau^{3,1}| \mathbf{u}_3(P_3, \tilde{P}_1, \tilde{P}_3) \cdot \mathbf{n}_{3,1}, \end{aligned} \tag{9}$$

$$\begin{aligned} u_{3,4}^{1/2} &\equiv \frac{1}{2} |\partial\tau^{3,4}| \mathbf{u}_3(P_3, \tilde{P}_1, \tilde{P}_3) \cdot \mathbf{n}_{3,4} \\ &= -\frac{1}{2} |\partial\tau^{4,3}| \mathbf{u}_4(P_4, \tilde{P}_2, \tilde{P}_3) \cdot \mathbf{n}_{4,3} ds. \end{aligned} \tag{10}$$

To eliminate three auxiliary variables, we solve the system (9)–(10) recalling the condition on the linearity of pressure in the quadrilateral region:

$$\tilde{P}_1 = \text{Linear extrapolation}(\tilde{P}_2, \tilde{P}_3, P_3). \tag{11}$$

Eliminating the auxiliary pressures results in local non-linear problems for estimation of fluxes over half-edges based on cell-center pressures, constrained by Eqs. 9–11.

<sup>2</sup>For L-method on quads, there are two possible choices of interaction regions to define flux across each half-edge (see Fig. 3 to the right). Optimal choice can be determined post hoc based on the effective stencils generated by the method [3]. For most cases, the choice of stencil is of secondary importance, and the current study therefore uses a pre-set choice of interaction region orientations.

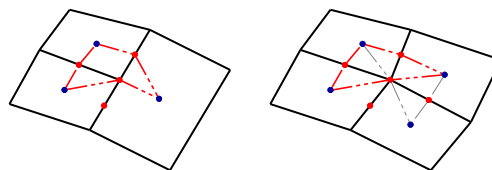


Fig. 3 Interaction regions for MPFA L-method. Configuration with a hanging node (left) and two possible interaction regions for computing the flux across the upper half-edge for a quadrilateral grid (right)

As in the preceding section, these local non-linear problems can be solved efficiently with a Newton iteration.

The method MPFA-L method defined above for quadrilateral grids can be naturally extended to more general grids with hanging nodes (see Fig. 3 on the left).

For the cells along the boundary of the domain where there are only two points in each interaction region, we revert to simpler two-point flux approximation. For further details on the construction of the MPFA L-method, we refer to [3].

### 3.3 Non-linear estimation of coarse scale velocity

To close the coarse problem, we need a way to resolve solve local non-linear systems: (8) for TPFa and Eqs. 9–11 for MPFA. This requires defining the procedure of computing velocity from the local pressure gradient. The general relation can be expressed in the form

$$\mathbf{u} = F(\nabla P). \tag{12}$$

Plugging this equation into the local computation of fluxes results in local non-linear systems, which in turn give rise to the global non-linear system through the total mass conservation (6).

The operator  $F$  defined in Eq. 12 is called a data-estimation operator in HMM terminology [23]. In this paper, we let  $F$  represent either the empirical upscaled Forchheimer’s law, or a finite element approximation of the Navier-Stokes’ equations described in Section 2.2. While the first choice links the CVHMM formulation to analytical single-scale formulations for non-linear flows, the latter results in a fully discrete multiscale method which demonstrates the full capability of the CVHMM framework. We review both choices below.

#### 3.3.1 Velocity estimation by Forchheimer’s law

The Forchheimer’s law is a common approximation of non-linear flow in porous medium which adds an inertial term to the linear Darcy’s law. It can be defined as

$$(A^{-1} + \beta|\mathbf{u}|)\mathbf{u} = -\nabla P, \tag{13}$$

where  $A$  is the linear (Darcy’s) coefficient related to permeability (obtained by solving the linear Stokes equation on

the same geometry), and  $\beta$  is the non-linear (Forchheimer’s) coefficient that can be obtained from experiments [30] or numerically [39]. When using the Forchheimer’s approximation in CVHMM, the data-estimation operator (12) can be defined as the solution to Eq. 13 for a given  $\nabla P$  at a given coarse scale location. Note, that this step does not involve fine-scale computations, but still leads to local non-linear systems. The original papers on the MPFA L-method considered only Darcy’s law—the discretization presented in the preceding section is thus the relevant generalization to non-Darcyan flows.

### 3.3.2 Velocity estimation by fine-scale finite element computation

In a fully discrete version of CVHMM, the function  $F$  from (12) is determined from upscaling of the flow field  $\mathbf{v}$  of the Navier-Stokes solution on the pore scale geometry by Eq. 5. The forcing function required to complete fine scale (4) is equated to the negative coarse-scale pressure gradient:

$$\tilde{\mathbf{f}} = -\nabla P. \tag{14}$$

This approach is consistent with homogenization [26] theory.

For the computational stability of fine-scale method, we re-scale the cell problem to the unit square and denote the rescaled components of the domain as  $\beta_1$ ,  $\sigma_1$  and  $\omega_1$  for fluid part, solid part and full cell respectively. The fine-scale domain is thus magnified  $\varepsilon^{-2}$  times. The scaled fine-scale problem must be solved by a suitable numerical method; we consider a low-order finite element formulation. The unknown and test functions are represented by the lowest-order Taylor-Hood basis (TH1) on the triangulated domain  $\beta_1$  (see Fig. 1). The functions are equipped with essential boundary conditions: periodic on the external boundaries of the square  $\omega_1$  and no-flow ( $\mathbf{v} = 0$ ) on the boundary with  $\sigma_1$ . The finite element problem reads: Find a pair of unknown functions  $(\mathbf{v}, p)$  (in TH1), that solve

$$a((\mathbf{v}, p), (\mathbf{w}, q)) = L(\mathbf{w}, q), \tag{15}$$

for all  $(\mathbf{w}, q)$  (in TH1), where

$$a((\mathbf{v}, p), (\mathbf{w}, q)) = \int_{\beta_1} \varepsilon^{-2} \mu \nabla \mathbf{v} : \nabla \mathbf{w} - p \nabla \cdot \mathbf{w} + q \nabla \cdot \mathbf{v} + \varepsilon^{-1} \rho \nabla \mathbf{v} \cdot \mathbf{w} dx \tag{16}$$

$$L(\mathbf{w}, q) = - \int_{\beta_1} \tilde{\mathbf{f}} \cdot \mathbf{w} dx. \tag{17}$$

Note that in (16), the dimensional constants from (4) are scaled with  $\varepsilon$  to preserve dimensionless groups appropriately to homogenization theory.

In our implementation, the formulation (15) is solved directly by non-linear PDE solver in the software package FENiCS [29].

The coarse-scale flow velocity for each principal direction  $\mathbf{n}$  are then estimated by formula (5) that in the notation of the fine scale can be written as

$$u_{\mathbf{n}} = \int_{\beta_1} \mathbf{v} \cdot \mathbf{n} dx, \tag{18}$$

where  $\mathbf{n}$  is a unit normal.

The period  $\varepsilon$  in Eq. 18 determines the separation of scales, and while it is defined precisely in synthetic examples of this paper, it corresponds to the representative elementary volume size used for fine scale simulation.

Equations 15 and 18 define the data estimation operator (12) for the fully discrete CVHMM. This approximation remains consistent with analytical homogenization results [26] and therefore ensures convergence properties of the method. The numerical verification of convergence can be found in the Appendix.

We note that although the focus herein is on a Navier-Stokes based fine-scale solver, the fully discrete HMM framework can also be applied with other pore-scale models such as pore-network models, as applied in [21, 22] or Lattice-Boltzmann methods.

### 3.4 Algorithm

With all the building blocks in place, what remains is to describe the algorithm coupling coarse-scale and fine-scale computations. The non-linearities in the system can in part be resolved on local interaction regions, but the global coarse-scale system is still non-linear in terms of the cell center pressures. We apply Newton’s method, with each iteration consisting of the following steps:

1. Assemble the vector that represents the out-flux (6) from each cell given  $P$  and their derivatives (the Jacobian) with respect to cell-center pressures.

The assembly of both the vector and the Jacobian is done by summing up the contributions from the interaction regions. For each region perform the following steps:

- (a) Find the auxiliary pressures so that continuity (8)-(10) is satisfied for every half-edge by solving local non-linear systems.
- (b) For each sub-region apply the data-estimation operator (12)

Fine 1 Apply the coarse pressure gradient to the local fine scale in each part of the control volume interaction region.

Fine 2 Solve the fine-scale problem for this geometry and pressure gradient (15).

Fine 3 Integrate the solution and apply required scaling to get the flux vector in the region (18).

Fine 4 To speed up computation, it is convenient to store previously the computed fluxes and recover them from an interpolation map instead of recomputing on every iteration.<sup>3</sup>

- (c) Solve equations for step 1a to obtain the fluxes across half-edges  $u_{i,j}$ .
  - (d) Add signed computed fluxes  $u_{i,j}$  across each half-edge to the out-flux of its neighboring cells.
  - (3) Perturb the pressures in the interaction regions and repeat steps (a)–(b) to find the contributions to the Jacobian matrix by finite differences.
2. Perform a Newton step to reduce mismatch between observed out-fluxes and the right-hand-side of Eq. 6.
  3. Repeat the procedure until the algorithm has converged.

The same algorithm can be applied to a standard upscaling which can be beneficial when the flow regime is presumed to be a priori known, e.g., using a data-estimation operator defined in Section 3.3.1.

The data-estimation operator in step 1b of the algorithm is then replaced by an algebraic computation, but will also require local solves of Eq. 13 for the local pressure gradients.

Both methods can leverage computations for flow regimes and pore geometries similar to ones already considered, by tabularization and interpolation. The main difference is that by making fewer assumptions, the fully discrete multiscale approach naturally adapts to flow regimes outside the precomputed range and also captures the non-trivial non-linear coupling between the Darcy and pore scale.

## 4 Numerical study of non-linearity in applications

One of the main advantages of the CVHMM framework discussed in this paper is that it can seamlessly handle non-linearities by automatically upscaling them from the physical simulation on the sub-Darcy scale without a priori assumptions on the structure of the upscaled constitutive laws. In this section, we consider three applications where standard Darcy's law approximations are insufficient. The first two examples involve near-well flow in the subsurface, with domains that are respectively uniform and fractured. For the fractured domain, we highlight the ability of the

method to adapt when it comes to computational effort. The third example is intended to investigate a manufactured fine-scale structure where directionally dependent resistance can occur. While we consider synthetic fine-scale geometries in these examples, pore-scale images are available both for geological and industrial porous media.

### 4.1 Near-well flow in homogeneous domain

Due to the radial structure of the flow field, near-well flow is commonly characterized by high flow rates, correspondingly high pressure gradients, and thus potentially non-linear flow effects. As noted earlier, the corresponding reduction of flow rates compared to the linear case can be hard to model. There are several papers which have developed tailored approaches to handle Forchheimer-type non-linearities in near well regions resulting in semi-analytical solutions with variable density effects [12] and special formulations for standard reservoir grids [24]. In contrast to the classical methods, CVHMM constitutes a framework that can handle different nonlinear flow relations depending on the fine-scale physics including (fully-discrete) multiscale and (classical) upscaled.

Currently, advances in imaging of well cores can be combined with resistivity measurements of the rock to estimate pore structure around a well [37]. Motivated by these results, we show how the CVHMM framework is capable of adapting to varying flow rates throughout the near-well domain using fully discrete HMM formulation.

Furthermore, our implementation of fully discrete method automatically tabulates the upscaled (non-linear) behavior observed in the domain. The numerical upscaling can be used to derive a Forchheimer's type approximation of the constitutive law (13) for the studied porous medium. As part of this example, we also compare how the choice of flow approximation influences the result of simulation.

Consequently, this numerical example is split in three parts. In the first part, we state all the assumptions and configurations used in the numerical experiments. In the second part (Section 4.1.2), we solve the postulated problem using a fully discrete CVHMM with a FEM approximation on the fine scale. In the third part (Section 4.1.3), we demonstrate the usage of CVHMM framework for the cases when the upscaled constitutive relationships are readily available.

The upscaled constitutive relationships used in Section 4.1.3 are calculated to be consistent with the numerical upscaling in Section 4.1.2.

In general, the same principles can be applied to derive other multiscale methods within CVHMM framework to include e.g. faster approximation of fine scale response using machine learning [19] or semi-statistical upscaling models [21].

<sup>3</sup>In our implementation, we use the quadratic interpolation in 2D when the mismatch between constant- and linear-interpolation-based approximation of fluxes is higher than a given threshold.

### 4.1.1 Example setup

We consider a rectangular domain that extends 64 centimeters away from a well perforation (see Fig. 5a). The flow in the well region is assumed to be driven by the pressure drop between the well and part of reservoir outside the computational domain that is less effected by near-well flow effects. The domain size is relatively small and will in a practical situation be dominated by the well. The external boundary condition is therefore set according to the pressure profile around a point source, given by

$$P = -a \log r + b, \tag{19}$$

where  $r$  is the distance from the point source, while the constants  $a = 8000$  and  $b = 7997.5$  (both in dimensionless units) are set to give a pressure drop of about one atmosphere over the  $x$ -dimension of the domain. To capture the expected pressure profile, the grid is logarithmically refined close to the well.

The non-linear effects will naturally depend on the fluid viscosity and the pore geometry (through the Reynolds number). Here, we set the intrinsic properties of the fluid equal to those of water at normal conditions. The 2D porous structure is created by randomly distributing round grains as shown in Fig. 4 with porosity of about 49%. The structure is assumed to be periodically repeated with each period spanning half a millimeter in each direction. For linear flow, the grain structure corresponds to a permeability on the order of 32 Darcy.

The values corresponding to the pore-scale assumptions in the problem set-up are similar to sand-column experiments reported in [32]. At low pressure drops, the experiments justified the Darcy’s law. Here, we impose pressure

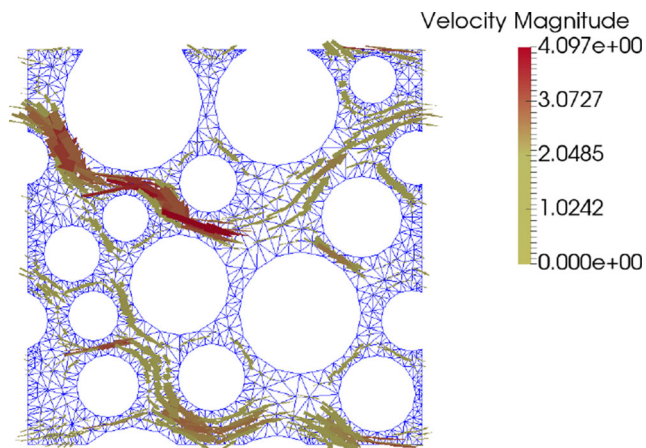
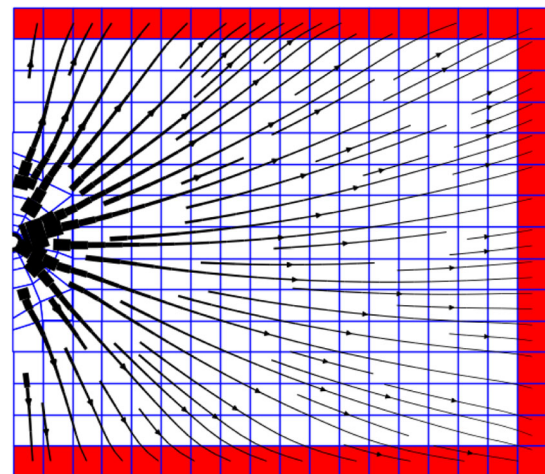


**Fig. 4** Fine-scale discretization of one period of pore geometry with a flow solution shown as arrows for homogeneous near-well flow example

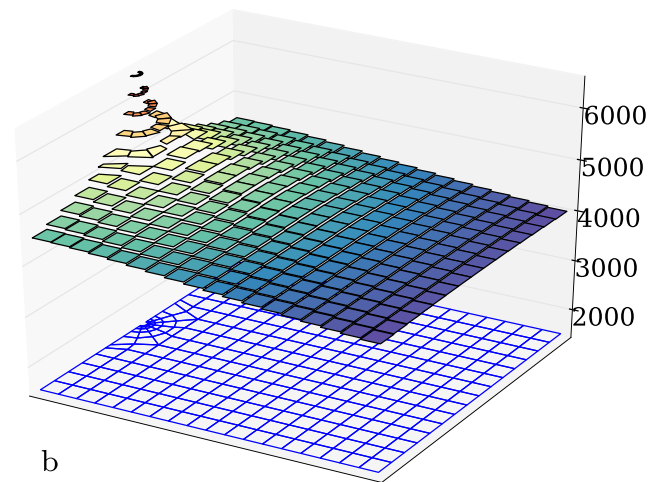
gradients which are about two orders of magnitude larger and thus expect non-linear behavior of the solution.

### 4.1.2 Fully discrete CVHMM

The solution to the fully discrete multiscale non-linear problem is given on Fig. 5. As expected, the near-well region experiences the highest flow rates and hence the most pronounced non-linear inertia effects. If we make the assumption of linear flow, this significantly reduces resistance to flow in the immediately vicinity of the well, and, since all fluid has to pass through this region to reach the well, higher flow rates throughout the domain compared to the fully resolved simulation. Figure 6a shows the



a



b

**Fig. 5** The solution for a near-well flow in homogeneous domain driven by pressure drop in dimension-less coordinates. a: Interpolated flow lines, also showing cells where pressure boundary condition is enforced. b: Pressure values in the control volume grid (negative part of z-axis are used for display of the original grid)

difference between linear (e.g., ignoring the interior-term in the fine-scale simulations) and non-linear flow. We observe some asymmetry in the solution, which we attribute to the slight anisotropy of the fine-scale structure. In terms of the pressure values, the difference between linear and non-linear flow is on the order of 0.5%, as seen from Fig. 6b. The difference in fluxes (at least locally) is, however, substantial. This can be visually observed by plotting the flux rates used during multi-scale data estimation against their Darcy's approximations (see Fig. 7). The relative discrepancies go up to 8% compare to the linear model (see Fig. 7b).

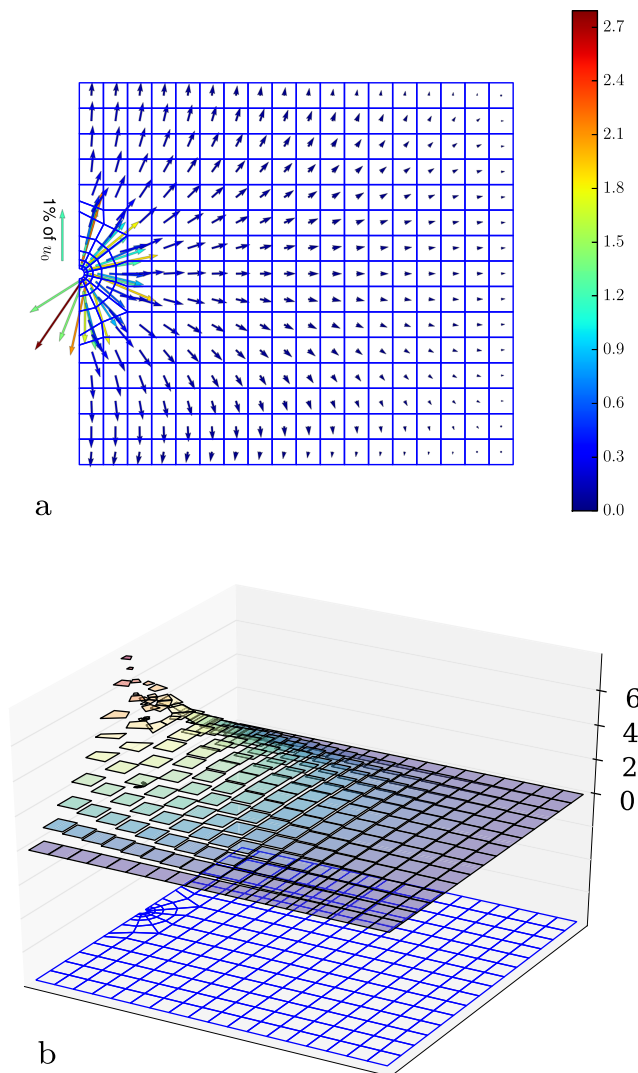


**Fig. 6** The difference between linear and non-linear solutions for near-well flow in a homogeneous domain. **a** Average difference in flow velocity for each cell scaled relative to 1% of average in-flux density ( $u_0$ ). For the sake of visualization, the arrows have been scaled such that the actual deviation is proportional to the length of the arrow squared. **b** Difference in pressure scaled to 1/1000 compare to reference pressure drop (negative part of z-axis are used for display of the original grid)

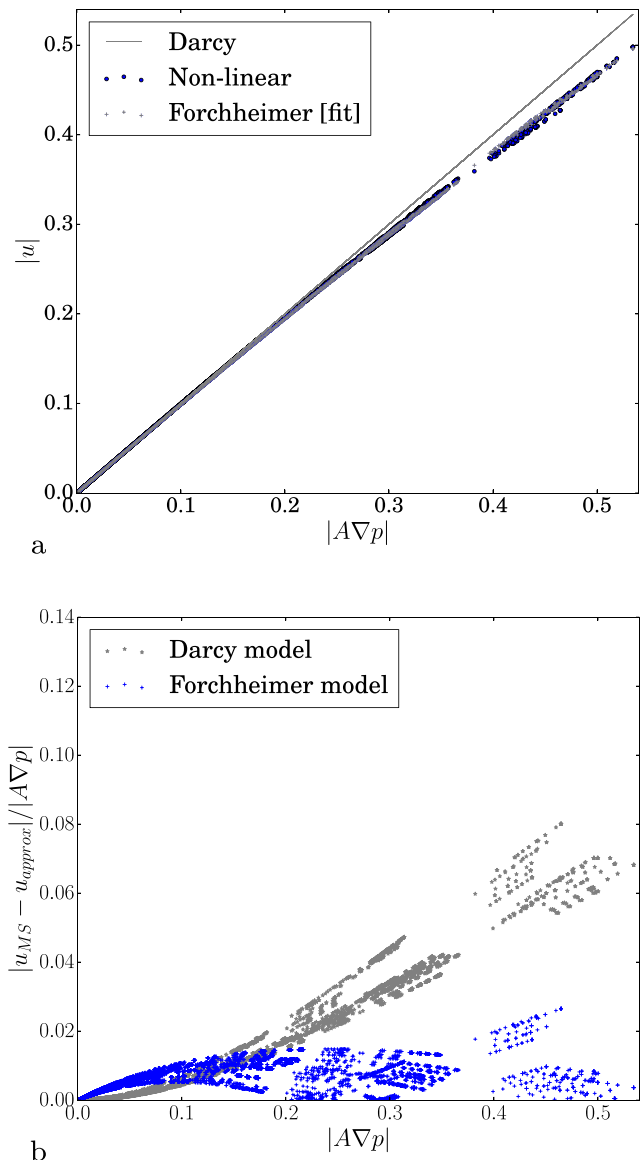


**Fig. 7** Relation between fluxes and the product of (estimated) permeabilities and pressure gradients. All the fine-scale data estimation points used for solving the coarse scale problem compared the linear relation (Darcy's law), and the best fit obtained with a Forchheimer relation (**a**). Relative differences between the fluxes estimated by multiscale solution and the two empirical models (**b**)

The flows observed during data estimation correspond to Reynolds numbers of up to 4.8,<sup>4</sup> which is above critical for nonlinear effects under laboratory conditions [30].

These errors translate to deviations of the course flux densities of over 2% compare to the computed density of the flow form the well (see Fig. 6a).

<sup>4</sup>The Reynolds number is estimated using formula from [55] putting the average grain diameter as the reference length.

The points resulting from the fine-scale simulation results demonstrate a well-known curved behavior of the fluxes observed both experimentally [30] and numerically [38]. Therefore, it is of interest to see whether the non-linear effects can be captured by the constitutive Forchheimer’s equation used to describe such non-linear curves. To that end, Fig. 7 also shows the best fit between the data from the fine scale simulations and the Forchheimer’s law (13), where  $\beta$  is obtained by least-square regression between (13) and the fine-scale simulation results. We observe that in this case, the numerical fluxes are in good, albeit not perfect, agreement with the Forchheimer relation with relative difference below 2% (see Fig. 7b). As one can expect from Eq. 13, the velocity magnitude is not a unique curve of  $|A\nabla P|$ , but a scatter. That is because the non-linear inertial effects are not directly influenced by the permeability and can be adequately approximated by a scalar  $\beta$  (see, e.g., [38]). Figure 7b also reveals another threat of direct parameter fitting. That is the relative error in Forchheimer model is actually larger than the error in the linear model near zero.

For a general heterogeneous media, the parameter  $\beta$  must be tuned to the different flow configurations, that in general are unknown in advance. The CVHMM approach with a pore-geometry fine-scale solver can be considered a way to determine the parameters for the relevant flow regime. We emphasize that the strength of the non-linear effect, and its spatial variation in this example, was automatically captured through the two-scale simulation.

#### 4.1.3 CVHMM with upscaled flow behavior

Considering the homogeneous set-up of this example, we can derive effective equations to relate the flow and the pressure gradients, by tuning of a single non-linear parameter  $\beta$  as discussed in the previous subsection. In this part of the example, we use the effective Forchheimer’s model plotted in Fig. 7 to demonstrate a CVHMM as a single-scale non-linear solver.

Here, we use the Forchheimer’s law (13) with  $\beta$  estimated numerically as the flux approximation in CVHMM and solve the same problem in the near-well region. Qualitatively the flow and pressure pattern for the CVHMM with Forchheimer’s approximation of flow to pressure relation is well approximated, and the results are visually similar to the fully discrete multiscale simulation results from Fig. 5. Therefore, we consider the difference between the solution with Forchheimer’s approximation and the fully discrete multiscale solution (see Fig. 8). As expected, both the velocity and the pressure are better matched compared to the case of linear approximation (see Fig. 6). The pressure is matched within a per mile in most of the domain.

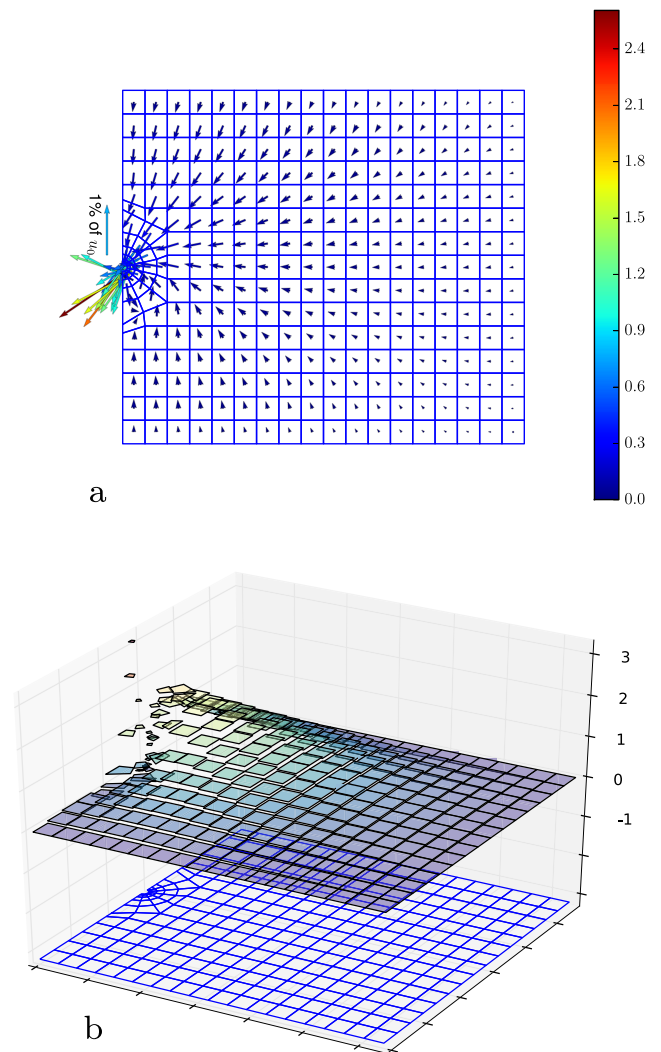
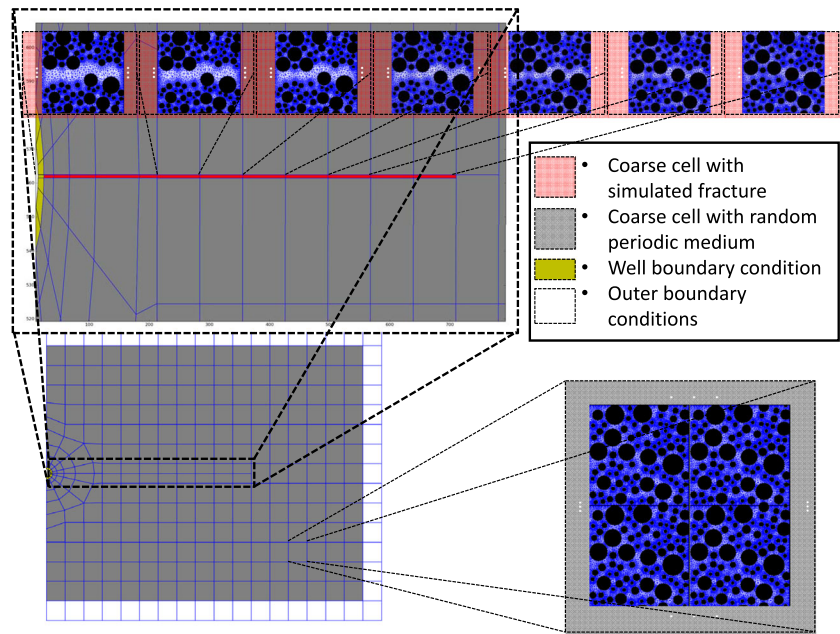


**Fig. 8** The difference between Forchheimer-based and fully discrete multiscale solutions for near-well flow in a homogeneous domain. **a** Average difference in flow velocity for each cell scaled relative to 1% of average in-flux density ( $u_0$ ). For the sake of visualization, the arrows have been scaled such that the actual deviation is proportional to the length of the arrow squared. **b** Difference in pressure scaled to 1/1000 compared to the reference pressure drop (negative part of z-axis are used for display of the original grid)

The Forchheimer-based approximation works well on average, but the anisotropic structure of the micro-scale is not captured by the scalar (not tensor) approximation of  $\beta$  in (13). This can be observed in the asymmetric structure of the mismatch in Fig. 8a. Larger errors near the well perforation for Forchheimer model can be also attributed to wrong resolution of components normal to the main flux direction. A more complex Forchheimer model could be considered to fully capture these effects.

The obvious advantage of using Forchheimer approximation as constitute relation is offloading the expensive

**Fig. 9** Coarse-scale computational domain for near-well flow example with a fracture. Zoomed portions depict porous media structures composed of random round grains and simulated fracture



fine-scale computations to a separate parameter estimation step, here requiring tuning of a single parameter. In many situations, this classical technique is more preferable than fully discrete multiscale method. As illustrated in this section, the CVHMM framework can due to its modular design, seamlessly accommodate a rich class of constitutive relations for the fine-scale behavior.

#### 4.2 Computational adaptivity in low-permeable domain with a fracture

Next, we consider a near-well region where the local pore geometry is tighter and non-linear effects are confined to fractures. Fracture permeability is commonly estimated by an assumption of flow between parallel plates, where the permeability is proportional to the aperture squared [17]. Irregularities in the fracture walls and filling material are accounted for by a reduction in the effective aperture, while non-linear flow effects can again be represented by a Forchheimer term. In practice, both the reduction of aperture and the non-linear term in Forchheimer's law requires tuning of parameters.

In this example, we avoid such assumptions on the resistance to flow, and instead compute the effective flow rates by CVHMM. The general setup is similar to that in the previous section. However, the domain is now heterogeneous in the sense that a single fracture is introduced in the middle of the domain, extending from the well as shown in Fig. 9. Fractures extending

from the well are frequently occurring from mechanical stresses induced by the drilling and completion processes. We make a conceptual model of a fracture based on perturbing an initial grain configuration, as might occur for an unconsolidated or weakly consolidated porous medium (see, e.g., [41]). Our fracture geometry is created by moving grains apart in  $y$ -direction starting from the initial random configuration. Compared to the initial configuration, the fracture permeability, e.g., assuming linear flow, is about 15 times higher along the fracture, and slightly less than the initial value perpendicular to the fracture. The reduction in fracture aperture away from the well perforation is controlled by varying the distance by which the grains are moved; the used distribution of fracture width is shown in Fig. 9. The fracture is also represented on the coarse-scale grid by the insertion of narrow cells along the fracture path (see Fig. 9). We note that this produces hanging nodes, that are readily handled by the coarse discretization. Again, the grid is logarithmically refined close to the well. For the non-linear effects to be confined to the fracture, the grain structure outside the fracture is defined as denser than that of Section 4.1, specifically, it corresponds to permeability of about 5 Darcy (see Fig. 9). The boundary conditions are taken equal to those in the previous section.

The solution to the problem with a fracture is shown in Fig. 10. As in previous example, the highest flow rates are observed around the source. However, in contrast with homogeneous case, the flow is to a large extent focused around the fracture.

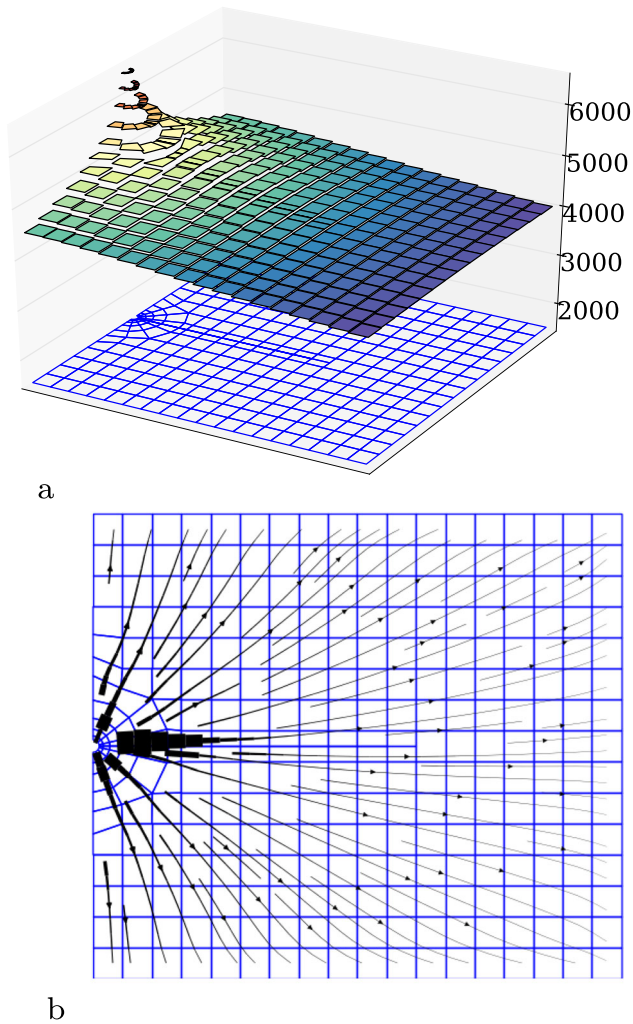


**Fig. 10** The solution for a near-well flow with fracture driven by pressure drop in dimension-less coordinates. **a** Cell center pressures (with the grid plotted below). **b** Interpolated flow lines)

Figure 11b shows relative difference in flux between linear and non-linear model which is plotted for all cells against their x-coordinate. One can observe outstanding values corresponding to the fracture where the linear model, which neglects added non-linear drag, over-predicts the flow-rate up to 25%.

The discrepancies observed around the source are attributed to the coarse system response to the non-linearity in the fracture.

The local non-linear effects in the fracture also correspond to about 1% over-prediction of the pressure (see Figure 11a). Notice that the highest discrepancy in pressure happens for both the fracture-occupied and surrounding cells especially near the well perforation where fracture aperture is highest and the flow is fastest. For a medium with a fracture the inaccuracy of the linear prediction is more pronounced than what produced in the previous example.

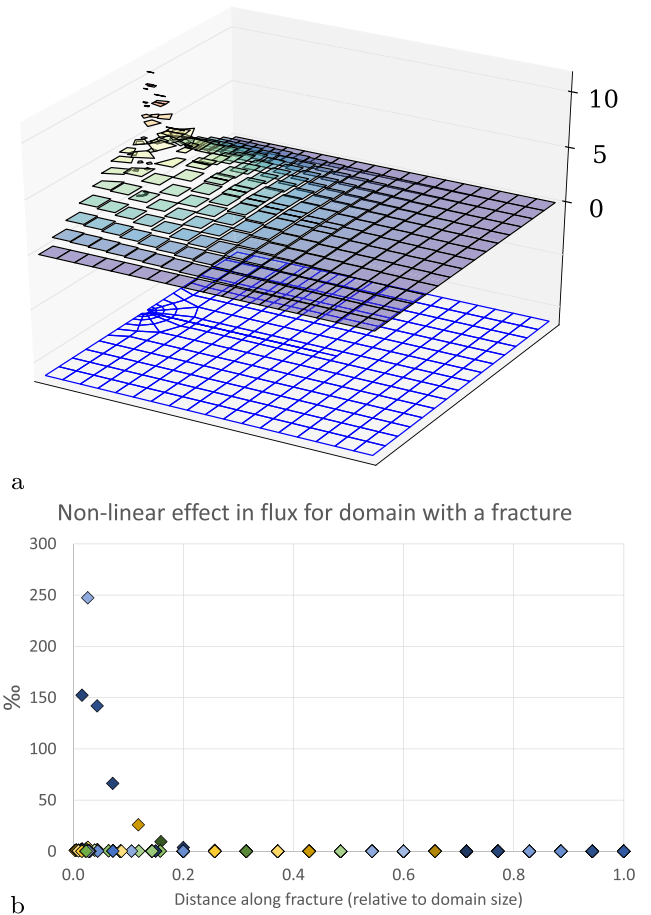


**Fig. 11** Non-linear effect observed for domain with a fracture. **a** Difference in pressure, scaled to 1/1000 compared to reference pressure drop (with the grid plotted below). **b** Difference in fluxes averaged over cells scaled by maximum flux. The absolute values of fluxes are plotted against the distance along the fracture scaled by the length of the domain. The plotted values correspond to both cells containing the fracture and cells with tight porous medium for which the effect due to non-linearity is negligible

The non-linear effects also have significant impact on the computational cost of the methods. Figure 12 shows the computational time spent on constructing the local MPFA fluxes and their derivatives, including the cost of the fine-scale Navier-Stokes solve, in each cell. Cells in the fracture, and in the immediate vicinity of the well, experience higher non-linearity, and an associated high computational cost. Conversely, cells with little flow also require less computations since our implementation caches the results of fine-scale computations for later reuse. The figure thus illustrates the power of CVHMM to dynamically adapt computational effort to the relevant parts of the domain.

While applying the method to a realistic 3D pore geometry would likely increase the time of solving

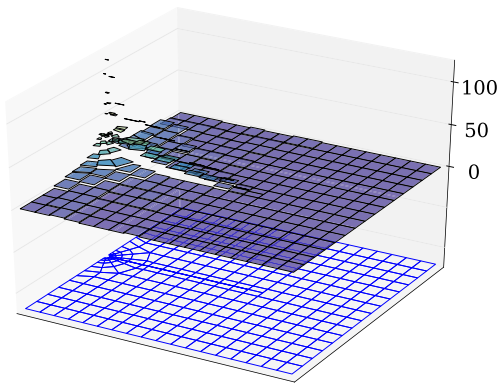


**Fig. 12** Computational time associated with the local problems arising from MPFA discretization (including fine-scale solves). For each coarse cell, average time spent for surrounding interaction regions is displayed in seconds. The underlying grid is shown below for reference

individual local problems it will not influence other parts of the multiscale method due to heterogeneous structure of the method formulation. Thus, the qualitative distribution of computational effort would be similar to Fig. 12.

### 4.3 Direction-dependent flow for non-circular grains

In our final example, we apply the CVHMM framework to study a case where the fine-scale geometry induces a flow which is not only directionally dependent, but which will also change value under flow reversal. It is well known that the drag coefficient of a streamlined body is dependent on the flow direction. The fine-scale domain depicted in Fig. 13 contains solid inclusions expected to give different resistance to flow depending on the flow direction. We therefore expect that the upscaled conductivity is different for flow going from the left to the right or vice versa, and have designed the pore-scale geometry to enhance

this effect. To quantify these effects, we consider a strip-shaped  $9 \times 4$  2D domain in which there is no-flow boundary condition on top and bottom and the pressure is set on the left and the right side to  $p_l$  and  $p_r$  respectively (see Fig. 13). While this case is not representative of porous rocks, this type of grain structures is of interest for industrial porous media, such as filters.

Our set-up is similar to the earlier work of [33] where non-reversible flow was also observed. Unlike this earlier work where parametrizations were derived explicitly for specific cases of porous media, we emphasize that CVHMM realizes a single integrated method for automatic upscaling. This simulation is therefore aimed at verifying that CVHMM can handle this kind of flow regimes, including flow reversal.

As in the previous example, the fluid is water. We assume that the periodic structure depicted on Fig. 13 is  $1 \text{ mm}^2$ , which results in Darcy's permeability of order  $10^3$  Darcy. On the coarse scale, the flow is driven by pressure drop of 32 kPa which is equivalent to water head of 3.3 m. This pressure drop is applied on the distance of 53 centimeters.

As in the previous example, relatively high permeability combined with fast flow results in significant discrepancy with the linear model of around 25% (see Table 1). Additionally for this case, we observe that the magnitude of flux changes depending on the direction in which the pressure drop is applied being higher when flow goes in streamlined direction, right to left in Fig. 13. For the considered scenario the relative pressure drop is about 4.5% (3.3% compare to linear). Numerical experiments indicate that the discrepancy decreases with decrease of the pressure drop. For instance for half the pressure drop, the directional dependency decreases to 3.5% (see Table 1).

Figure 14 shows how non-linear effects are up-scaled from the solution of fine-scale problem. The figure shows

**Fig. 13** A 2D porous medium structure where matrix is composed of stream-lined bodies. A zoomed-in part depicts discretization of fluid part of a local cell problem with color map of a pressure solution

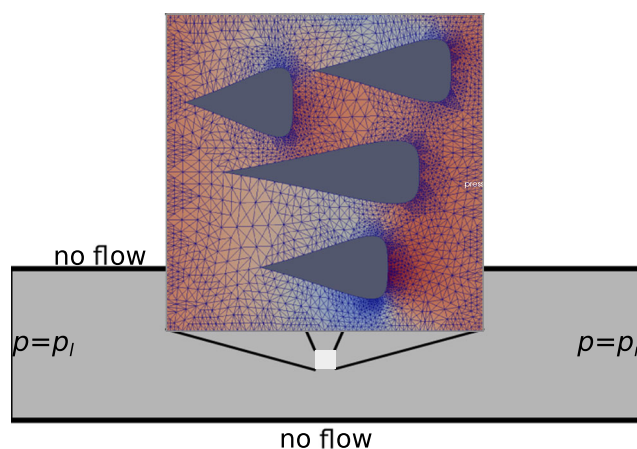


**Table 1** Comparison of total fluxes through industrial porous media for linear and non-linear direction-dependent cases

Pressure drop magnitude	Linear flux (%)	Non-linear along (right-to-left) (%)	Non-linear reverse (left to right) (%)
The reference drop	100	77	74
Half the reference drop	50	43	42

For the sake of comparison the linear flux under reference pressure drop is taken to be 100%. The fluxes corresponding to 50% pressure drops are also shown to highlight the differences of non-linearities depending on flow velocities

correlation between Darcy’s permeability ( $x$ -axes) and the flow velocity obtained by solving non-linear fine-scale problem in CVHMM ( $y$ -axes). The point cloud is created of the fine-scale simulations used to solve the coarse the problem case presented in this sub-section. In Fig. 14, there is apparent trend of growing discrepancy between linear and non-linear model for higher velocities. Moreover, given the spread of values for each  $A\nabla P$ , it is impossible to define a simple one-parametric non-linear upscaling. When we fix the direction of the flow to  $x$ -axis (red stars in Fig. 14), one can still observe multiple values of flow velocities. These two groups correspond to positive and negative directions of the flow respectively. While non-trivial fit-for-purpose models with multiple tunable parameters such as [33] are required to capture such regime in a static Darcy-scale model, the CVHMM captures the effects automatically. Naturally, the multiscale simulation that is not provided with an a priori parametrization of fluxes might require more fine-scale runs, but it also focuses the effort on the regimes relevant for the particular problem as shown in the previous example. The dynamic computation is also able to resolve effects for media configurations that cannot be represented by simple geometrical lattices giving CVHMM superior flexibility.

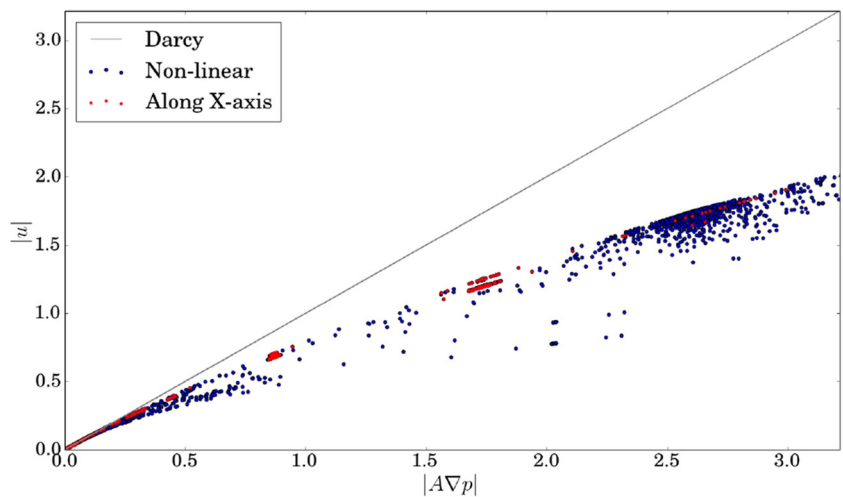
### 5 Conclusions

In this paper, we have presented a generalized multi-point version of control volume heterogeneous multiscale method (CVHMM) for resolving non-linear flows in porous media. The CVHMM approach ensures mass conservation on the coarse scale of the problem while seamlessly handling non-linear processes arising from the fine-scale physics.

Compared to previous CVHMM approaches [8, 9], the presented method consistently handles anisotropy of the underlying pore structure. Moreover, the new approach is able to handle general grid configurations, including hanging nodes, which makes it a relevant tool for polyhedral grids with local refinement required in near-well regions.

We emphasize that CVHMM stands for a framework of methods suitable for flows with challenging non-linear physics. Essentially, the framework presented in this paper provides a constructive approach for MPFA-type methods for single-phase flows with inertia effects, which are underrepresented in the literature. In particular, we have shown that it can be used with both a pre-selected upscaled model (on the example of the Forchheimer’s law) and a discrete fine-scale solver (on the example of Navier-Stokes’ FEM on the pore scale). While the latter is the main intended

**Fig. 14** Comparison of permeability with non-linear flow function for porous structure from Fig. 13. Blue dots represents data points for all grid edges, red stars only edges in the  $x$ -direction. Velocity of 2 corresponds to  $Re = 200$



purpose of the framework, the ability to act as a single-scale non-linear-flow solver allows to gradually adopt the method for practical problems where the flow model is well known or the pore-scale information is not available.

The utility of the new method is verified with focus on the more complex fully discrete configuration. For that, we have considered a number of test cases involving flows in near-well regions, fractured domains, and industrial porous media. The examples highlight that our fully discrete approach seamlessly upscales cases where the flow regime is not known in advance.

As expected, for problems with relatively weak non-linearity the single-scale method (based on the Forchheimer's approximation) gives reasonably close match to the fully-discrete method. The approximation requires tuning of a single non-linear parameter, thus showing computational advantage of CVHMM based on upscaling.

In more general cases, however, earlier parametric upscaling methods require complex a priori analysis and manual fitting of multiple parameters [33, 38, 39]. In contrast, the fully discrete CVHMM is directly applicable throughout the whole range of fluid flow regimes. In the final example we also expose that permeability can change as the flow direction is reversed, a fact that is rarely mentioned in literature.

The natural drawback is that the multiscale method spends more computational effort compare to closed-form upscaling. This would be even more pronounced when considering realistic 3D pore geometries which are out of scope of this paper. In order to optimize the computations, we implement a bespoke design of fine-scale solver with on-demand computation and interpolation maps based on previous fine-scale results. The computational adaptivity is confirmed by the test with a fracture where challenging non-linear effects are only observed locally (e.g., due to particular fine-scale geometries). In that case, the method localizes the computational effort to the interaction regions requiring special non-linear treatment.

With the continuous improvements in technology for imaging and design of porous media, numerical upscaling of pore-scale flow will be of increasing importance in the future. The computational framework presented herein offers an attractive tool for such simulations, coupling pore- and Darcy-scale models under varying flow conditions with little or no heuristic user interaction.

**Acknowledgments** SA acknowledges the Research Council of Norway and the industry partners; ConocoPhillips Skandinavia AS, BP Norge AS, Det Norske Oljeselskap AS, Eni Norge AS, Maersk Oil Norway AS, DONG Energy A/S, Denmark, Statoil Petroleum AS, ENGIE E&P NORGE AS, Lundin Norway AS, Halliburton AS, Schlumberger Norge AS, Wintershall Norge AS of The National IOR Centre of Norway for support. SA also thanks Anna Kvashchuk, Trine Solberg Mykkeltvedt and Kundan Kumar for helpful discussions during the preparation of the manuscript. The authors thank the reviewers

for constructive criticism that helped to improve and better frame the paper.

**Open Access** This article is distributed under the terms of the Creative Commons Attribution 4.0 International License (<http://creativecommons.org/licenses/by/4.0/>), which permits unrestricted use, distribution, and reproduction in any medium, provided you give appropriate credit to the original author(s) and the source, provide a link to the Creative Commons license, and indicate if changes were made.

## Appendix: Numerical validation of the fully-discrete method

In this appendix, we validate newly formed MPFA-based fully discrete CVHMM and highlight its superiority compared to two-point multiscale methods. The method falls within the HMM family and thus assumes scale separation. The method is not designed to approximate the full fine-scale solution, but to use the fine-scale information for estimation of the missing coarse-scale relations consistently. Thus, the numerical examples study the error propagation to the coarse scale.

We consider tests on two different pore geometries, which allow us to highlight different properties of the method. The first test considers a pore structure from [9] which created challenges for two-point method due to orientation of its upscaled permeability tensor. In the second test, we focus on two-scale convergence under refinement of both the coarse and the fine grid.

### Consistency on arbitrary porous media

It is well known [1] that TPFA is convergent only if the principal axis of the permeability coincide with the principal directions of the grid. As shown in [9], this inconsistency carries over to HMM-approaches based on the two-point flux. The MPFA methods were developed to overcome the consistency errors of TPFA, and the purpose of this test is to verify that a similar improvement can be seen for the corresponding multiscale methods (see schematics in Fig. 2). To that end, we revisit the experiment presented in [9]. We consider a randomly generated pore structure (see Fig. 1) which is extended periodically to form the fine scale of the whole computational domain. Based on the homogenization theory [26], the coarse linear problem can be defined in the closed form as

$$-\nabla \cdot A \nabla P = f. \quad (20)$$

We benchmark the numerical method by comparing a coarse-scale numerical solution on the unit square to a chosen function of the form:

$$P = (0.5 - |x - 0.5|) (0.5 - |y - 0.5|). \quad (21)$$

**Table 2** Experimental order of convergence of the fully discrete CVHMM for different uniform coarse refinement steps (H1 ref.); the values that are larger than the theoretically expected are highlighted in italics

H1 ref.	TPFA				MPFA			
	0 h-refs	1 h-refs	2 h-refs	3 h-refs	0 h-refs	1 h-refs	2 h-refs	3 h-refs
1	<i>1.8</i>							
2	<i>1.8</i>	<i>1.7</i>	<i>1.7</i>	<i>1.7</i>	<i>2.0</i>	<i>1.8</i>	<i>1.8</i>	<i>1.8</i>
3	0.8	0.9	0.9	0.9	<i>2.1</i>	<i>1.9</i>	<i>1.9</i>	<i>1.9</i>
4	0.0	0.1	0.1	0.1	0.1	<i>1.8</i>	<i>1.9</i>	<i>1.9</i>
5	0.0	0.0	0.0	0.0	− 0.2	<i>1.7</i>	<i>1.9</i>	<i>1.9</i>

The table contains results for two different quadrature rules TPFA or MPFA. For each of them, the fine scale problem is solved using FEM discontinuities with zero to three uniform refinements (0 h-refs–3 h-refs) the fine-scale grid from Fig. 1

To compute the source term  $f$  corresponding to the analytical solution (21), we first estimate  $A$  by solving the cell problem from Fig. 1 numerically on a highly refined fine-scale grid (3 uniform refinements), and then substitute  $A$  and Eqs. 20 and 21.

The initial coarse-scale grid has a resolution of  $H = 1/4$  and fine grid starts with triangulation shown in Fig. 1b; we then consider uniform refinements on the coarse and the fine scale. Due to linearity of the system, the period  $\varepsilon$  does not play an explicit role in the error, but the size of fine-scale discretization should be understood relative to the period.

The comparison of the experimental orders of convergence with respect to coarse-grid resolutions for both two-point flux method and the multi-point flux CVHMM are presented in Table 2. While the two-point method suffers from inconsistency errors and fails to converge the multi-point method achieves the order of convergence of around 1.9 after only two fine-scale refinements. Table 2 gives a clear indication of the consistency errors of TPFA-based method, that can be seen in rows 3–5. Regardless of the fine-scale refinement, the final error stays almost the same and method stops converging.

On contrary, for the case of MPFA-based method, two h-refinements is sufficient (the last two columns in Table 2) to reach the optimal order of convergence with respect to considered coarse scale grids.

The observed order of convergence with respect to the coarse scale discretization is close to the second order observed for single-scale MPFA methods with a discontinuous right hand side [3]. The  $L_2$  norm of the error has the same qualitative behavior and is omitted for brevity.

We note that for single-scale problems, the consistency errors in the two-point flux to some extent can be overcome by orienting the grid along the principal axes of the permeability (see, e.g., [1]). Such techniques are however less viable in two-scale simulations, where the equivalent permeability is not known a priori.

### Two-scale convergence

The pore structure of Fig. 1 requires a highly resolved grid to conform to the geometry. As a result, the error from the solution of cell problems gives only marginal contribution to the overall error after the first  $h$ -refinement.

Here, we consider an example from Fig. 2 where a coarse-scale grid is aligned with the  $xy$ -axis of the fine-scale unit cell, which has simple diagonal grain arrangement

that is purposely misaligned with the coarse geometry. Moreover, the fine-scale geometry can be meaningfully meshed by a relatively coarse grid. This leaves room for multiple grid refinements on the fine scale and allows us to study the interplay between coarse- and fine-scale convergence.

Again, we consider the linear coarse-scale (20). The numerical errors are computed as the difference of fully,discrete numerical solutions and the chosen analytical expression on the unit square:

$$P(x, y) = \sin(\pi x) \sin(\pi y), \quad (x, y) \in (0, 1) \times (0, 1) \quad (22)$$

The right hand side in Eq. 20 in this example is computed as follows. First the tensor  $A$  is estimated by numerical upscaling: we solve fine-scale cell problem numerically on a very fine grid (after four refinements). Then, the semi-analytical source term  $f$  is computed knowing  $P$  and  $A$ , that can be written as:

$$f = (A_{11} + A_{22}) \sin(\pi x) \sin(\pi y) - 2A_{12} \cos(\pi x) \cos(\pi y) \quad (23)$$

We note that the analytical solution is smooth, and we therefore expect high rates of convergence.

To study the interaction between the errors, we refine both the coarse- and fine-scale grid and compare the approximated pressure solutions with the analytical solution (22) in the  $H_1$  semi-norm (measured in terms of the coarse

**Table 3** Experimental order of convergence (EOC) for the test in Section 1 in terms of coarse- and fine-scale refinements

	0 h-refs	1 h-refs	2 h-refs	3 h-refs	4 h-refs	
EOC of the discrete $H^1$ semi-norm of the error with respect to coarse-scale grid refinements:						
1	1.5	2.0	2.0	1.9	1.9	
2	0.9	2.5	2.1	2.0	2.0	
3	0.4	0.8	2.6	2.2	2.0	
4	0.1	-0.4	0.3	2.6	2.0	
5	0.0	-0.1	-0.4	0.0	2.0	
EOC of the discrete $H^1$ semi-norm of the error with respect to fine-scale grid refinements:						
	0 H-refs	1 H-refs	2 H-refs	3 H-refs	4 H-refs	5 H-refs
1	0.2	0.8	2.3	2.8	2.2	2.1
2	0.0	-0.1	-0.5	1.3	2.0	1.8
3	0.0	0.0	-0.1	-0.5	1.8	2.1
4	0.0	0.0	-0.1	-0.2	-0.8	1.1

The values that are larger than the theoretically expected are highlighted in italics

grid). Note again, that choosing  $L_2$  norm yields the same qualitative behavior. Table 3 shows the experimental order of convergence of the  $H^1$ -seminorm (convergence of the pressure gradients) as both the coarse- and the fine-scale grid are refined. As can be seen from the table, both the fine- and coarse discretization errors contributes to the overall accuracy, i.e., the expected order of convergence with respect to each scale is only achieved when the other scale is sufficiently refined.

These results are in perfect agreement with the error analysis for the two-point flux method in [9].

**Publisher's Note** Springer Nature remains neutral with regard to jurisdictional claims in published maps and institutional affiliations.

## References

1. Aavatsmark, I.: Interpretation of a two-point flux stencil for skew parallelogram grids. *Comput. Geosci.* **11**(3), 199–206 (2007). <https://doi.org/10.1007/s10596-007-9042-1>
2. Aavatsmark, I., Barkve, T., Bøe, O., Mannseth, T.: Discretization on unstructured grids for inhomogeneous, anisotropic media. Part I: Derivation of the methods. *SIAM J. Sci. Comput.* **19**(5), 1700–1716 (1998). <https://doi.org/10.1137/S1064827595293582>
3. Aavatsmark, I., Eigestad, G.T., Mallison, B.T., Nordbotten, J.M.: A compact multipoint flux approximation method with improved robustness. *Numer. Methods Partial Differ. Equ.* **24**, 1329–1360 (2008). <https://doi.org/10.1002/num.20320>. <http://onlinelibrary.wiley.com/doi/10.1002/num.20320/abstract>
4. Abdulle, A.: The finite element heterogeneous multiscale method: a computational strategy for multiscale PDEs. *Mult. Scales Probl. Biomath. Mech. Phys. Numer.* **31**, 133–181 (2009)
5. Abdulle, A.: A priori and a posteriori error analysis for numerical homogenization: a unified framework. In: Damilamian, A., Miara, B., Li, T. (eds.) *Multiscale Problems*, vol. 16, pp. 280–305. World Scientific (2011). <https://doi.org/10.1142/8267>. [http://anmc.epfl.ch/Pdf/abdulle\\_cam\\_final\\_pr.pdf](http://anmc.epfl.ch/Pdf/abdulle_cam_final_pr.pdf). [http://www.worldscientific.com/doi/abs/10.1142/9789814366892\\_0009](http://www.worldscientific.com/doi/abs/10.1142/9789814366892_0009)
6. Abdulle, A., Budáč, O.: An adaptive finite element heterogeneous multiscale method for stokes flow in porous media. *Multiscale Model. Simul.* **13**(1), 256–290 (2015). <https://doi.org/10.1137/130950136>
7. Abdulle, A., Budáč, O.: A reduced basis finite element heterogeneous multiscale method for stokes flow in porous media. *Comput. Methods Appl. Mech. Eng.* **307**, 1–31 (2016). <https://doi.org/10.1016/j.cma.2016.03.016>
8. Alyaev, S., Keilegavlen, E., Nordbotten, J.: Multiscale simulation of non-Darcy flows. In: CMWR, pp. 1–8. <http://cmwr2012.cce.illinois.edu/Papers/SpecialSessions/HybridMultiscaleModelsInSubsurfaceFlowandTransport/Alyaev.Seregy.pdf> (2012)
9. Alyaev, S., Keilegavlen, E., Nordbotten, J.M.J.: Analysis of control volume heterogeneous multiscale methods for single phase flow in porous media. *MMS* **12**(1), 335–363 (2014). <https://doi.org/10.1137/120885541>
10. Andrá, H., Combaret, N., Dvorkin, J., Glatt, E., Han, J., Kabel, M., Keehm, Y., Krzikalla, F., Lee, M., Madonna, C., Marsh, M., Mukerji, T., Saenger, E.H., Sain, R., Saxena, N., Ricker, S., Wiegmann, A., Zhan, X.: Digital rock physics benchmarks-part II: Computing effective properties. *Comput. Geosci.* **50**, 33–43 (2013). <https://doi.org/10.1016/j.cageo.2012.09.008>

11. Andrà, H., Combaret, N., Dvorkin, J., Glatt, E., Han, J., Kabel, M., Keehm, Y., Krzikalla, F., Lee, M., Madonna, C., Marsh, M., Mukerji, T., Saenger, E.H., Sain, R., Saxena, N., Ricker, S., Wiegmann, A., Zhan, X.: Digital rock physics benchmarks-Part I: Imaging and segmentation. *Comput. Geosci.* **50**, 25–32 (2013). <https://doi.org/10.1016/j.cageo.2012.09.005>
12. Aulisa, E., Ibragimov, A., Valko, P., Walton, J.: Mathematical framework of the well productivity index for fast Forchheimer (non-Darcy) flow in porous media. *Math. Models Methods Appl. Sci.* **19**(8), 1241–1275 (2009). <http://citeseerx.ist.psu.edu/viewdoc/download?doi=10.1.1.182.5461&rep=rep1&type=pdf>
13. Balhoff, M., Mikelić, A., Wheeler, M.F.: Polynomial filtration laws for low Reynolds number flows through porous media. *Transp. Porous Media* **81**(1), 35–60 (2010). <https://doi.org/10.1007/s11242-009-9388-z>
14. Balhoff, M., Wheeler, M.: A predictive pore-scale model for non-Darcy flow in porous media. *SPE J.* **14**, 9 (2009). <https://doi.org/10.2118/110838-PA>. <http://www.onepetro.org/mslib/servlet/onepetro/preview?id=SPE-110838-PA>
15. Balhoff, M.T., Thomas, S.G., Wheeler, M.F.: Mortar coupling and upscaling of pore-scale models. *Comput. Geosci.* **12**(1), 15–27 (2008). <https://doi.org/10.1007/s10596-007-9058-6>
16. Barree, R.D., Conway, M.W.: Beyond beta factors: a complete model for Darcy, Forchheimer, and Trans-Forchheimer flow in porous media. In: *Proceedings of SPE Annual Technical Conference and Exhibition*, p. 8. <https://doi.org/10.2523/89325-MS> (2004)
17. Berkowitz, B.: Characterizing flow and transport in fractured geological media: a review. *Adv. Water Resour.* **25**(8), 861–884 (2002). [https://doi.org/10.1016/S0309-1708\(02\)00042-8](https://doi.org/10.1016/S0309-1708(02)00042-8)
18. Blunt, M.J., Bijeljic, B., Dong, H., Gharbi, O., Iglauer, S., Mostaghimi, P., Paluszny, A., Pentland, C.: Pore-scale imaging and modelling. *Adv. Water Resour.* **51**, 197–216 (2013). <https://doi.org/10.1016/j.advwatres.2012.03.003>
19. Chan, S., Elsheikh, A.H.: A machine learning approach for efficient uncertainty quantification using multiscale methods. *J. Comput. Phys.* **354**, 493–511 (2018)
20. Chen, Z., Lyons, S.L., Qin, G.: Derivation of the Forchheimer Law via Homogenization, pp. 325–335 (2001)
21. Chu, J., Engquist, B., Prodanovic, M., Tsai, R.: A multiscale method coupling network and continuum models in porous media I: steady-state single phase flow. *Multiscale Model. Simul.* **10**(2), 515–549 (2012). <https://doi.org/10.1137/110836201>
22. Chu, J., Engquist, B., Prodanovic, M., Tsai, R.: A multiscale method coupling network and continuum models in porous media II: single-and two-phase flows. In: *Advances in Applied Mathematics, Modeling, and Computational Science*, pp. 161–185. Springer (2013)
23. Weinan, E., Engquist, B.: The heterogeneous multiscale methods. *Comm. Math. Sci.* **1**(1), 87–132 (2003)
24. Ewing, R.E., Lazarov, R.D., Lyons, S.L., Papavassiliou, D.V., Pasciak, J., Qin, G.: Numerical well model for non-Darcy flow through isotropic porous media. *Comput. Geosci.* **3**(3-4), 185–204 (1999). <https://doi.org/10.1023/A:1011543412675>. [papers2://publication/uuid/94680680-1A1A-4E3C-BDDE-D9182D7F93EC](https://pubs.opengroup.org/standards/info/94680680-1A1A-4E3C-BDDE-D9182D7F93EC)
25. Faigle, B., Helmig, R., Aavatsmark, I., Flemisch, B.: Efficient multiphysics modelling with adaptive grid refinement using a MPFA method. *Comput. Geosci.* **26**, 625–636 (2014). <https://doi.org/10.1007/s10596-014-9407-1>
26. Hornung, U.: *Homogenization and Porous Media*, vol. 6. Springer, Berlin (1997)
27. Iliev, O., Kirsch, R., Lakdawala, Z., Rief, S., Steiner, K.: *Currents in Industrial Mathematics*. Springer, Berlin (2015). <https://doi.org/10.1007/978-3-662-48258-2>
28. Lao, H.W., Neeman, H.J., Papavassiliou, D.V.: A pore network model for the calculation of non-Darcy flow coefficients in fluid flow through porous media. *Chem. Eng. Commun.* **191**(10), 1285–1322 (2004). <https://doi.org/10.1080/00986440490464200>
29. Logg, A., Mardal, K., Wells, G.: *Automated Solution of Differential Equations by the Finite Element Method Lecture Notes in Computational Science and Engineering*, vol. 84. Springer, Berlin (2012). <https://doi.org/10.1007/978-3-642-23099-8>
30. Macini, P., Mesini, E., Viola, R.: Laboratory measurements of non-Darcy flow coefficients in natural and artificial unconsolidated porous media. *J. Pet. Sci. Eng.* **77**(3-4), 365–374 (2011). <https://doi.org/10.1016/j.petrol.2011.04.016>
31. Mattila, K., Puurtinen, T., Hyväluoma, J., Surmas, R., Myllys, M., Turpeinen, T., Robertsén, F., Westerholm, J., Timonen, J.: A prospect for computing in porous materials research: Very large fluid flow simulations. *J. Comput. Sci.* **12**, 62–76 (2016). <https://doi.org/10.1016/j.jocs.2015.11.013>
32. Mavis, F., Wilsey, E.: A study of the permeability of sand. *University of Iowa Studies in Engineering (Bulletin 7)*, pp. 1–29. <http://ir.uiowa.edu/cgi/viewcontent.cgi?article=1007&context=uisie> (1936)
33. McClure, J.E., Gray, W.G., Miller, C.T.: beyond anisotropy: examining Non-Darcy flow in asymmetric porous media. *Transp. Porous Media* **84**(2), 535–548 (2010). <https://doi.org/10.1007/s11242-009-9518-7>
34. Mehmani, Y., Balhoff, M.T.: Bridging from pore to continuum: a hybrid mortar domain decomposition framework for subsurface flow and transport. *Multiscale Model. Simul.* **12**(2), 667–693 (2014). <https://doi.org/10.1137/13092424X>
35. Narsilio, G.A., Buzzi, O., Fityus, S., Yun, T.S., Smith, D.W.: Upscaling of Navier-Stokes equations in porous media: theoretical, numerical and experimental approach. *Comput. Geotech.* **36**(7), 1200–1206 (2009). <https://doi.org/10.1016/j.compgeo.2009.05.006>
36. Ovaysi, S., Piri, M.: Direct pore-level modeling of incompressible fluid flow in porous media. *J. Comput. Phys.* **229**(19), 7456–7476 (2010). <https://doi.org/10.1016/j.jcp.2010.06.028>
37. Oyewole, E., Garcia, A.P., Heidari, Z.: A new method for assessment of directional permeability and conducting pore network using electric conductance in porous media. In: *SPWLA 57th Annual Logging Symposium* (2016)
38. Peszynska, M., Trykozko, A.: Pore-to-core simulations of flow with large velocities using continuum models and imaging data. *Comput. Geosci.* **17**(4), 623–645 (2013). <https://doi.org/10.1007/s10596-013-9344-4>
39. Peszynska, M., Trykozko, A., Sobieski, W.: Forchheimer law in computational and experimental studies of flow through porous media at porescale and mesoscale. *Math. Sci. Appl.* **32**, 463–482 (2010)
40. Ramstad, T., Idowu, N., Nardi, C., Øren, P.E.: Relative permeability calculations from two-phase flow simulations directly on digital images of porous rocks. *Transp. Porous Media* **94**(2), 487–504 (2012). <https://doi.org/10.1007/s11242-011-9877-8>
41. Santillán, D., Mosquera, J.C., Cueto-felgueroso, L.: Fluid-driven fracture propagation in heterogeneous media: Probability distributions of fracture trajectories. *Phys. Rev. E.* **96**(5), 1–10 (2017). <https://doi.org/10.1103/PhysRevE.96.053002>
42. Scheibe, T.D., Perkins, W.A., Richmond, M.C., McKinley, M.I., Romero-Gomez, P.D.J., Oostrom, M., Wietsma, T.W., Serkowski, J.A., Zachara, J.M.: Pore-scale and multiscale

- numerical simulation of flow and transport in a laboratory-scale column. *Water Resour. Res.* **51**(2), 1023–1035 (2015). <https://doi.org/10.1002/2014WR015959>
43. Sheng, Q., Thompson, K.: Dynamic coupling of pore-scale and reservoir-scale models for multiphase flow. *Water Resour. Res.* **49**(9), 5973–5988 (2013). <https://doi.org/10.1002/wrcr.20430>
44. Skjetne, E., Auriault, J.L.: New insights on steady, non-linear flow in porous media. *Eur. J. Mech. - B/Fluids* **18**(1), 131–145 (1999). [https://doi.org/10.1016/S0997-7546\(99\)80010-7](https://doi.org/10.1016/S0997-7546(99)80010-7)
45. Skjetne, E., Kløv, T., Gudmundsson, J.: Experiments and modeling of high-velocity pressure loss in sandstone fractures. *SPE Journal* (March):61–70. <https://doi.org/10.2118/69676-PA> (2001)
46. Sun, T., Mehmani, Y., Balhoff, M.T.: Hybrid multiscale modeling through direct substitution of pore-scale models into near-well reservoir simulators. *Energy Fuels* **18**(5), 5828–5836 (2012). <https://doi.org/10.1021/ef301003b>
47. Swift, G.W., Kiel, O.G.: The prediction of gas-well performance including the effect of non-Darcy flow. *J. Petrol. Tech.* **14**(07), 791–798 (1962)
48. Tomin, P., Lunati, I.: Hybrid multiscale finite volume method for two-phase flow in porous media. *J. Comput. Phys.* **250**, 293–307 (2013). <https://doi.org/10.1016/j.jcp.2013.05.019>. <http://linkinghub.elsevier.com/retrieve/pii/S0021999113003513>
49. Tomin, P., Lunati, I.: Spatiotemporal adaptive multiphysics simulations of drainage-imbibition cycles. *Comput. Geosci.* **20**(3), 541–554 (2016). <https://doi.org/10.1007/s10596-015-9521-8>
50. Wang, Y., Li, X., Zheng, B., Zhang, Y.X., Li, G.F., Wu, Y.F.: Experimental study on the non-Darcy flow characteristics of soil-rock mixture. *Environ. Earth Sci.* **75**(9), 756 (2016). <https://doi.org/10.1007/s12665-015-5218-5>
51. Whitaker, S.: Flow in porous media {II}: the governing equations for immiscible, two-phase flow. *Transp. Porous Med.* **1**, 105–125 (1986)
52. Whitaker, S.: The forchheimer equation: a theoretical development. *Transp. Porous Media* **25**, 27–61 (1996)
53. Wildenschild, D., Sheppard, A.P.: X-ray imaging and analysis techniques for quantifying pore-scale structure and processes in subsurface porous medium systems. *Adv. Water Resour.* **51**, 217–246 (2013). <https://doi.org/10.1016/j.advwatres.2012.07.018>
54. Zaretskiy, Y., Geiger, S., Sorbie, K., Förster, M.: Efficient flow and transport simulations in reconstructed 3D pore geometries. *Adv. Water Resour.* **33**(12), 1508–1516 (2010). <https://doi.org/10.1016/j.advwatres.2010.08.008>
55. Zeng, Z., Grigg, R.: A criterion for non-darcy flow in porous media. *Transp. Porous Media* **63**(1), 57–69 (2006). <https://doi.org/10.1111/j.1439-0523.2006.01169.x>